Correlating charge movements with local conformational changes of a Na(+)-coupled cotransporter

Patti, Monica ; Forster, Ian C

Abstract: To gain insight into the steady-state and dynamic characteristics of structural rearrangements of an electrogenic secondary-active cotransporter during its transport cycle, two measures of conformational change (pre-steady-state current relaxations and intensity of fluorescence emitted from reporter fluorophores) were investigated as a function of membrane potential and external substrate. Cysteines were substituted at three believed-new sites in the type IIb Na(+)-coupled inorganic phosphate cotransporter (SLC34A2 flounder isoform) that were predicted to be involved in conformational changes. Labeling at one site resulted in substantial suppression of transport activity, whereas for the other sites, function remained comparable to the wild-type. For these mutants, the properties of the pre-steady-state charge relaxations were similar for each, whereas fluorescence intensity changes differed significantly. Fluorescence changes could be accounted for by simulations using a five-state model with a unique set of apparent fluorescence intensities assigned to each state according to the site of labeling. Fluorescence reported from one site was associated with inward and outward conformations, whereas for the other sites, including four previously indentified sites, emissions were associated principally with one or the other orientation of the transporter. The same membrane potential change induced complementary changes in fluorescence at some sites, which suggested that the microenvironments of the respective fluorophores experience concomitant changes in polarity. In response to step changes in voltage, the pre-steady-state current relaxation and the time course of change in fluorescence intensity were described by single exponentials. For one mutant the time constants matched well with and without external Na(+), providing direct evidence that this label reports conformational changes accompanying intrinsic charge movement and cation interactions.

DOI: https://doi.org/10.1016/j.bpj.2014.02.028

Correlating Charge Movements with Local Conformational Changes of a Na^+-Coupled Cotransporter

Monica Patti and Ian C. Forster*
Institute of Physiology and Zurich Center for Integrative Human Physiology, University of Zurich, Zurich, Switzerland

ABSTRACT To gain insight into the steady-state and dynamic characteristics of structural rearrangements of an electrogenic secondary-active cotransporter during its transport cycle, two measures of conformational change (pre-steady-state current relaxations and intensity of fluorescence emitted from reporter fluorophores) were investigated as a function of membrane potential and external substrate. Cysteines were substituted at three believed-new sites in the type IIb Na^+-coupled inorganic phosphate cotransporter (SLC34A2 flounder isoform) that were predicted to be involved in conformational changes. Labeling at one site resulted in substantial suppression of transport activity, whereas for the other sites, function remained comparable to the wild-type. For these mutants, the properties of the pre-steady-state charge relaxations were similar for each, whereas fluorescence intensity changes differed significantly. Fluorescence changes could be accounted for by simulations using a five-state model with a unique set of apparent fluorescence intensities assigned to each state according to the site of labeling. Fluorescence reported from one site was associated with inward and outward conformations, whereas for the other sites, including four previously indentified sites, emissions were associated principally with one or the other orientation of the transporter. The same membrane potential change induced complementary changes in fluorescence at some sites, which suggested that the microenvironments of the respective fluorophores experience concomitant changes in polarity. In response to step changes in voltage, the pre-steady-state current relaxation and the time course of change in fluorescence intensity were described by single exponentials. For one mutant the time constants matched well with and without external Na^+, providing direct evidence that this label reports conformational changes accompanying intrinsic charge movement and cation interactions.

INTRODUCTION

There is compelling evidence from the resolved crystal structures of secondary-active transporters that these membrane proteins adopt unique conformational changes during the transport cycle as substrates bind, translocate, and are released to the opposite side of the membrane (e.g., Forrest et al. (1)). However, the identified conformations provide only limited snapshots of the transport process without giving insight into the kinetics of the transitions between states. Indirect experimental evidence for the dynamic processes occurring comes from functional studies using techniques such as single-molecule fluorescence resonance energy transfer (2–4), electron parametric resonance (5), and time-resolved fluorometry (6–8). Moreover, these techniques allow observation of the protein behavior under more physiologically relevant conditions than those used for crystallography.

Electrogenic cotransporters offer a unique opportunity to study transport dynamics because one of the driving forces for transport, membrane potential, can be readily manipulated in real-time by means of the voltage-clamp technique. For electrogenic members of the SLC34 family of sodium-coupled phosphate cotransporters (NaPi-IIa, NaPi-IIb), the functional property of electrogenicity manifests itself as steady-state P_i-induced currents at a fixed membrane potential and pre-steady-state current relaxations evoked by rapid changes in membrane potential, as commonly observed in many electrogenic solute carriers (for review, see Forster et al. (9)).

Analysis of pre-steady-state relaxations led to the identification of voltage-dependent partial reactions in the transport cycle (Fig. 1 *A*), namely the empty carrier transition ($0 \leftrightarrow 1$) and Na^+ interactions ($1 \leftrightarrow 2$, $2 \leftrightarrow 3$, and $7 \leftrightarrow 0$) (9,10). Moreover, the presence of mobile charge movements that are resolvable in real-time on a macroscopic scale provides strong evidence for voltage-dependent conformational changes. Thus, in the absence of external driving cations, charge movements largely reflect transitions between inward and outward-facing conformations of the protein itself; the interaction of cations contributes further to the total charge movement as these ions purportedly move within the transmembrane electric field to and from their binding sites. However, from pre-steady-state current relaxation analysis alone it may be difficult to identify and localize conformational changes to specific regions of the protein because of the global nature of the assay. In summary, the link between charge movement—reported as an equivalent lumped charge moving through a fraction of the transmembrane electric field—and protein conformational change is at best indirect, especially if the charge movement arises from a concerted redistribution of many charges.

We have also applied voltage-clamp fluorometry (10–14) that yields information on local conformational changes in

Submitted November 26, 2013, and accepted for publication February 28, 2014.

*Correspondence: iforster@access.uzh.ch

Editor: Ernest Wright.

0006-3495/14/04/1618/12 $2.00

http://dx.doi.org/10.1016/j.bpj.2014.02.028

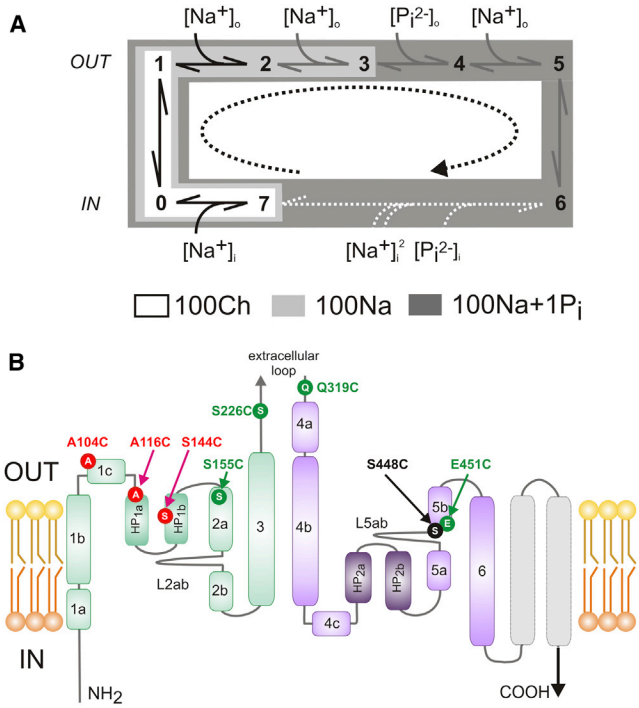

FIGURE 1 Kinetic scheme of NaPi-IIb transport cycle and sites of cysteine substitution. (*A*) An eight-state kinetic scheme describes the cotransport cycle. Under physiological conditions this proceeds in the direction shown (*dashed arrow*). The empty carrier transition ($0 \leftrightarrow 1$), Na^+ interactions ($1 \leftrightarrow 2$, $0 \leftrightarrow 7$) are assumed to be electrogenic (*black arrows*). In this study, three experimental conditions define the occupied states and interconverting partial reactions: 100 mM choline Cl (100Ch) (*white*); 100 mM NaCl (100Na) (*gray*); and 100 mM NaCl + 1 mM P_i (100Na+1P_i) (*dark gray*). For each condition, the relative occupancy of any state depends on the membrane potential. (*B*) Proposed secondary topology model (adapted from Fenollar-Ferrer et al. (23)) based on homology of human NaPi-IIa using the bacterial Na^+-dicarboxylate transporter, VcINDY (31) as template. Repeat units are shown colored (*green*, RU1; *violet*, RU2). Numbers indicate predicted α-helical stretches and transmembrane helices according to Fenollar-Ferrer et al. (23). Two additional transmembranes not considered in the homology model are also shown (*gray*). (*Circles*) Approximate location of the Cys substitution sites considered in this study: previously described sites (*green* (14), *black* (13)) and believed new sites in this study (*red*). To see this figure in color, go online.

specific regions of the protein. Time-resolved measurement of fluorometric emissions (voltage-clamp fluorometry offers a complementary tool to observe, indirectly, voltage- and substrate-dependent conformational changes (e.g., Cha et al. (15)). By labeling each substituted cysteine of a population of proteins with thiol-reactive fluorophores, changes in their microenvironment caused by local conformational changes will be reported as changes in the macroscopic fluorescence intensity resulting, for example, from collisional quenching of individual fluorophores (15). Because these measurements are made in real time, we can consider the fluorophore as a motion reporter at the chosen labeling site. We have previously used this technique to identify multiple cation interactions in the flounder NaPi-IIb (13) and mouse NaPi-IIc (12), and complementary movement of two reentrant domains during the transport cycle of flounder NaPi-IIb (14) and the putative release of cations at the cytosolic face of the protein (10).

Here, we investigate possible correlations between presteady-state charge movements and simultaneously measured changes in fluorescence intensity emitted from fluorophores covalently bound to selected sites in the flounder NaPi-IIb protein. The flounder isoform was chosen because of its high functional expression in *Xenopus* oocytes (e.g., Forster et al. (16)) and to allow comparison with previous structure-function studies (11,13,14). A direct correlation between the mobile charge movement and fluorescence would suggest that the fluorophore senses the same motion event as reported by the charge movement. We have previously reported that such a correlation exists over a limited range of membrane potentials for one labeled site in NaPi-IIb (13). This approach has been applied to other cation-coupled symporters (e.g., SGLT1 (7,8,17) and GAT1 (18)) to elucidate structure-function correlates during voltage-driven conformational changes. By restricting which conformational states the protein can occupy (for example, by defining the substrate availability and membrane voltage (Fig. 1 *A*)), we aimed to identify parts of the protein involved in empty carrier reorientation, cation interactions, and substrate translocation under physiological conditions. The choice of site should reflect its proximity to functionally important regions that undergo conformational changes in response to membrane potential changes and, ideally, satisfy our requirement that neither the Cys-substitution nor the thiol labeling should significantly alter the transport behavior. Four sites that fulfill these criteria were identified in a previous study (14); however, correlations between charge and fluorescence were not explored. Here, we introduce three believed-new sites (Fig. 1 *B*) to augment our functional mapping of local conformational changes in response to a globally induced state change by an externally applied step in membrane voltage.

MATERIALS AND METHODS

Solutions and reagents

Oocytes were incubated in a modified Barth's solution that contained 88 mM NaCl, 1 mM KCl, 0.41 mM $CaCl_2$, 0.82 mM $MgSO_4$, 2.5 mM $NaHCO_3$, 2 mM $Ca(NO_3)_2$, and 7.5 mM HEPES, adjusted to pH 7.5 with TRIS and supplemented with antibiotics doxycyclin and gentamicin (5 mg/L). The superfusing solutions contained (100Na solution), 100 mM NaCl, 2 mM KCl, 1.8 mM $CaCl_2$, 1 mM $MgCl_2$, and 10 mM HEPES, pH 7.4, adjusted with TRIS; 100Ch: same as for 100Na solution, but with equimolar replacement of NaCl with choline Cl. For intermediate Na^+ concentrations, 100Na and 100Ch were appropriately mixed to maintain the same osmolarity. Inorganic phosphate (P_i) was added to the superfusate from 1 M K_2HPO_4 and KH_2PO_4 stocks that were mixed to give pH 7.4. All standard reagents were obtained from either Sigma-Aldrich (St. Louis, MO) or Fluka (Buchs, Switzerland). MTSET (two-(trimethylammonium) ethylmethanethiosulfonate bromide) and MTS-TAMRA (2-((5(6)-tetramethylrhodamine)carboxylamino) ethyl methanethiosulfonate) were obtained from Biotium (Hayward, CA).

Site-directed mutagenesis and cRNA preparation

cDNA-encoding, wild-type (WT) flounder NaPi-IIb (GenBank/EMBL/DDBJ accession No. AAB16821) was subcloned into a vector containing the 5′ and 3′ UTRs from *Xenopus* β-globin to improve its expression in oocytes. Novel (to our knowledge) cysteines were introduced using the QuikChange site-directed mutagenesis kit (Agilent Technologies, Santa Clara, CA). The sequence was verified by sequencing (Microsynth, Balgach, Switzerland) linearized with *Xba*I. The cRNA was synthesized in the presence of Cap analog using the T3 Message Machine kit (Ambion, Austin, TX).

Expression in *Xenopus laevis* oocytes

Animal procedures and preparation of oocytes followed standard procedures (e.g., Patti et al. (10) and Andrini et al. (19)) and were in accordance with the Swiss Cantonal and Federal legislation relating to animal experimentation. Stage V–VI oocytes were selected, maintained in modified Barth's solution at 16°C, and injected with 50 nL of cRNA (200 ng/μL). Experiments were performed 4–5 days after injection.

^{32}P uptake

Control oocytes (NI) and oocytes expressing fNaPi-IIb WT and cysteine mutants (10–15 oocytes/group) were first allowed to equilibrate in 100Na without tracer. After aspiration of this solution, oocytes were incubated in 100Na containing 1 mM cold P_i and ^{32}P (specific activity 10 mCi mmol^{-1}). Uptake proceeded for 10 min and then oocytes were washed four times with ice-cold 100Ch containing 2 mM P_i, and lysed individually in 2% sodium dodecyl-sulfate for 10 min before addition of the scintillation cocktail. The amount of radioactivity in each oocyte was measured by scintillation counting.

Two electrode voltage-clamp

Standard two-electrode voltage-clamp hardware was used (GeneClamp, Model 500; Molecular Devices, Eugene, OR or TEC-10X; NPI, Tamm, Germany). Voltage-clamp control, data acquisition, and perfusion valve switching were all under software control using PCLAMP Ver. 8–10 software (Molecular Devices).

Determination of apparent P_i affinity

To determine the apparent affinity constant for P_i ($K_{0.5}^{Pi}$), the electrogenic response to different P_i concentrations added to the 100Na control solution was measured at a defined membrane potential. Oocytes were voltage-clamped to $V_h = -60$ mV and voltage steps were applied in the range -160 to $+60$ mV for typically 100 ms. To measure P_i-induced currents (I_{Pi}), the superfusate was switched from the control (100Na) solution to one containing a given concentration of P_i and when the holding current had reached a steady state, the voltage steps were repeated. The control data set was subtracted from the data set obtained in the presence of P_i to give I_{Pi} for each [P_i] and test voltage. Estimates of $K_{0.5}^{Pi}$ were obtained by fitting data with a form of the Michaelis-Menten equation given by

$$I_{P_i} = I_{P_i}^{\max}[P_i] \Big/ \left([P_i] + K_{0.5}^{P_i}\right) + I_{\mathrm{OFF}}, \qquad (1)$$

where I_{Pi}^{max} is the maximum current attainable, and I_{OFF} is a variable offset to account for uncoupled leak effects (20). To take account of the differences in expression levels between individual oocytes, data obtained from each oocyte were normalized to I_{Pi} recorded at -100 mV with 100Na and 1 mM P_i before pooling and fitting the data with Eq. 1.

Thiol modification by MTSET

MTSET were prepared from dry stock in water to give 1 M stock solution and kept at -20°C until required. This was further diluted before adding to 100Na or 100Ch to give the working concentration for determination of the reaction rate. MTSET was applied to the chamber with gravity feed via a 0.5-mm-diameter cannula positioned near the cell. During MTSET application, oocytes were kept at $V_h = -50$ mV. After washout, the P_i-induced current was remeasured. The effective second-order reaction rates were determined by fitting a single decaying exponential to the peak P_i-dependent current after a cumulative exposure time t, (I^t_{Pi}) determined following each successive MTS exposure,

$$I_{Pi}^{t} = \left(I_{Pi}^{0} - I_{Pi}^{\infty}\right)\exp(-ctk^{*}) + I_{Pi}^{\infty}, \qquad (2)$$

where I^0_{Pi} is the P_i response at $t = 0$, I^∞_{Pi} is the response at $t = \infty$, c is the concentration of MTS reagent (assumed to be in excess), and k^* is the effective second-order rate constant (21).

Voltage-clamp fluorometry

The voltage-clamp fluorometry apparatus comprised a two-electrode voltage-clamp (TEC-10CX; NPI, Tamm, Germany) and a laboratory-built fluorescence microscope as previously described in Virkki et al. (13), with the following changes:

1. For some experiments, we used an XF32 cube set (with 535DF35 excitation filter, 570DRLP dichroic mirror, and 596DF35 emission filter; Omega Optical, Brattleboro, VT).
2. Excitation was via a green LED light source (Luxeon LXHL-PM02; Philips Lumileds Lighting, San Jose, CA) driven by stabilized current source.
3. For labeling, oocytes were incubated in 0.4 mM MTS-TAMRA in 100Na and kept in the dark at 20°C for 5 min.

Voltage step protocols and pre-steady-state analysis

The protocol for recording pre-steady-state current and simultaneous fluorescence used voltage steps from $V_h = -60$ mV to voltages in the range -200 mV to $+200$ mV. Signals were averaged 20–40 fold and filtered at 500 Hz (4-pole Bessel). Pre-steady-state current relaxations were typically quantified for voltages in the range -180 mV $\le V \le 100$ mV where we could exclude contamination from endogenous Cl^- currents. Current relaxations were typically fitted with a multiple exponential function. The fastest component, which represents the linear capacitive charging of the oocyte membrane (typically 0.35–0.6 ms, depending on the oocyte), was subtracted from the total relaxation to obtain the NaPi-II-dependent component of transient current. For some oocytes, depending on voltage-clamp settling time, we obtained improved fits (as judged by the reported fit residual) by choosing a three-exponential algorithm. However, we routinely used a two-exponential fit to obtain the time constant for the main charge relaxation because fit results that were more consistent were obtained over the whole test voltage range. After subtraction of the fast capacitive component, the remaining current was numerically integrated to obtain the charge moved (Q) for a step from the holding potential to the test potential. The Q-V data were fitted with a Boltzmann function of the form given by

$$Q = Q_{\mathrm{hyp}} + Q_{\max} \Big/ \left(1 + \exp\left(z^{Q} e\left(V_{0.5}^{Q} - V\right)/kT\right)\right), \qquad (3)$$

where $V_{0.5}^{Q}$ is the voltage at which the charge is distributed equally between two hypothetical states, z^Q is the apparent valency of an equivalent charge that moves through the whole of the membrane field, Q_{max} is the

total mobile charge available, Q_{hyp} is the charge of the hyperpolarizing limit and is a function of V_h, and e, k, and T have their usual meanings. Each fluorescence recording was baseline-corrected relative to the value at $V_h = -60$ mV. After correction for any systematic loss of F as described previously in Virkki et al. (13), data from single oocytes were normalized to the predicted maximum change in fluorescence (ΔF_{max}) obtained in the solution that gave the highest ΔF and then pooled. ΔF_{max} was obtained from the ΔF-V data, which were fitted with the Boltzmann equation (Eq. 3, where Q was substituted with ΔF and the corresponding fit parameters are ΔF_{max}, z^F, and $V_{0.5}{}^F$). The time course of ΔF was described by fitting a single growing exponential function.

Data analysis and simulations

Curve fitting using Eqs. 1–3 was performed using GraphPad PRISM Ver. 4 for Windows, (GraphPad Software, San Diego, CA, www.graphpad.com). Data points are shown as mean ± SE. Error bars are not displayed if smaller than the graphical symbol. Kinetic simulations were performed using Berkeley MADONNA V8.0.2a8 software (www.berkeleymadonna.com).

RESULTS

Functional characterization of Cys mutants in flounder NaPi-IIb before and after thiol labeling

Three new sites in the flounder NaPi-IIb protein (Ala-104 Ala-116, and Ser-144) were chosen for cysteine substitution (Fig. 1 *B*) based on a previous structure-function study using the rat NaPi-IIa isoform (22), which suggested that this region of the protein might undergo unique conformation changes. When expressed in *X. laevis* oocytes, the mutants showed Na^+-dependent ^{32}P uptake and P_i-induced currents (I_{Pi}) in the presence of external Na^+ (100Na solution) under voltage-clamp that were comparable with WT levels (with $P_i = 1$ mM, typical magnitude for $I_{Pi} \geq 100$ nA at -50 mV) (data not shown). These assays confirmed that the substitutions were well tolerated. Furthermore, to establish whether mutagenesis had altered the basic cotransport kinetics, we determined the apparent affinity constant for P_i in 100Na ($K_{0.5}{}^{Pi}$) (see Materials and Methods) for each mutant. At -100 mV, the $K_{0.5}{}^{Pi}$ values were 0.07 ± 0.02 mM (A104C), 0.04 ± 0.02 mM (A116C), and 0.02 ± 0.01 mM (S144C), which were comparable with reported data for the WT (0.03 ± 0.01 mM) and previously described mutants (e.g., Virkki et al. (14)). We concluded that the Cys-mutagenesis had left the electrogenic transport mechanism intact.

In addition to tolerating the Cys substitution, we required that the substituted Cys be accessible for labeling and that this should not cause a significant deviation from WT behavior, as for previously reported substitutions at Ser-155, Ser-226, Gln-319C, and Glu-451 (14). We therefore examined the electrogenic behavior of the new mutants before and after exposure to MTSET or the thiol-reactive fluorophore MTS-TAMRA (see Fig. S1 in the Supporting Material). Mutants A104C and A116C showed insignificant change in I_{Pi} after exposure to these reagents (1 mM, 5 min; see Fig. S1 *A*). In contrast, S144C displayed a significant reduction in I_{Pi} (see Fig. S1 *B*). We characterized the loss of electrogenic transport function by exposing oocytes expressing S144C to MTSET for successive 1-min intervals and measured I_{Pi} after each exposure (Materials and Methods). The rate of decrease in I_{Pi} was dependent on the incubation medium (see Fig. S1 *C*). For exposure to MTSET in 100Ch, the effective second-order reaction rate (k^*) = 0.746 s^{-1} M^{-1}, whereas for incubation in 100Na, $k^* = 129$ s^{-1} M^{-1}, which was comparable to values we have previously reported (e.g., Virkki et al. (13)). The slow rate of modification in 100Ch indicated that this site was significantly less accessible in the absence of external Na^+ ions. Because S144C did not satisfy our experimental criterion, we did not investigate its properties further.

For mutants A104C and A116C, we next investigated whether incubation with MTS-TAMRA altered the characteristics of the pre-steady-state charge movements. Current relaxations were measured for each mutant in response to voltage steps with varying $[Na^+]_o$ from 0 to 100 mM. Analysis yielded the steady-state mobile charge distribution as a function of membrane potential (see Materials and Methods, and see Fig. S2). The parameters obtained from Boltzmann fits that describe the main features of the charge-voltage (Q-V) relations were generally close to those previously reported for the WT (14,19). However, there were small shifts in the absolute values of the midpoint voltage of the Q-V data ($V_{0.5}{}^Q$) (Table 1) after labeling and small (<10%) changes in the main relaxation time constant reported by

TABLE 1 Comparison of properties of midpoint voltages $V_{0.5}{}^Q$ and $V_{0.5}{}^F$

Parameter	WT	A104C	A116C	S155C*	S226C*	Q319C*	E451C*
$V_{0.5}{}^Q$ (mV)†	−11 ± 7	0.3 ± 1.4	2 ± 1	6 ± 3	−9 ± 4	−5 ± 4	−3 ± 5
$V_{0.5}{}^Q$ (mV)†	**n.d.**	**5 ± 2**	**−8 ± 1**	**-8 ± 5**	**2 ± 3**	**−5 ± 5**	**6 ± 3**
$V_{0.5}{}^F$ (mV)†	**n.a.**	**−27 ± 3**	**−16 ± 3**	**-34 ± 1**	**32 ± 3**	**35 ± 2**	**−12 ± 7**
$V_{0.5}{}^Q/\log[Na^+]_o$ (mV/decade)	122 ± 18	119 ± 8	93 ± 10	104 ± 12	91 ± 7	105 ± 8	129 ± 5
$V_{0.5}{}^Q/\log[Na^+]_o$ (mV/decade)	**n.d.**	**100 ± 12**	**116 ± 7**	**101 ± 14**	**102 ± 9**	**109 ± 8**	**131 ± 4**
$V_{0.5}{}^F/\log[Na^+]_o$ (mV/decade)	**n.a.**	**121 ± 7‡**	**94 ± 1**	**140 ± 5**	**58 ± 8**	**55 ± 3**	**99 ± 2**

Each entry is the mean ± SE for $n \geq 4$ for each construct. Key: n.a., not applicable; n.d., not determined. Bold entries indicate fitted parameters obtained after labeling with MTS-TAMRA.

*Data reported in Virkki et al. (14).

†Superfusion with 100 mM Na^+ (100Na).

‡Boltzmann fit performed from minimum of ΔF-V data to hyperpolarizing extreme (see text).

the fitting algorithm after MTS-TAMRA exposure (see Fig. S2 *B*). We found that the dependence of $V_{0.5}{}^{Q}$ on the concentration of external Na^+ ions ($[Na^+]_o$) gave similar limiting slopes when plotted against $\log_{10}[Na^+]_o$ and was close to the expected value ($\approx$120 mV/decade) (19) (Table 1). This finding confirmed that for A104C or A116C, neither the Cys substitution nor exposure to thiol-reactive reagents had significantly altered the external Na^+ interactions.

Changes in fluorescence intensity reported by cysteine mutants after labeling with MTS-TAMRA

When voltage steps were applied to either noninjected oocytes or WT NaPi-IIb, voltage-dependent changes in the emitted fluorescence intensity (ΔF) were not detected. However, for the labeled A104C and A116C, ΔF was resolved whose magnitude and polarity depended on the composition of the superfusion medium and the labeling site. For oocytes expressing A116C (Fig. 2 *A*), in the absence of external Na^+ (100Ch), equal and opposite 120 mV steps from the −60 mV holding potential induced ΔF of similar magnitude, with quenching of fluorescence occurring for the depolarizing step relative to the baseline value at −60 mV. The addition of 100 mM Na^+ (100Na) resulted in a larger ΔF for the depolarizing step and reduced ΔF for the hyperpolarizing step, thus resulting in a shift of the ΔF-V distribution along the voltage axis (Fig. 2 *B*, *right panel*). In contrast, the addition of 1 mM P_i had marginal effect on ΔF for depolarizing potentials compared with 100Ch, but further reduced the magnitude of ΔF for the hyperpolarizing step. Mutant A104C (Fig. 2 *A*, *upper*) also gave ΔF with all three superfusing conditions; however, unlike A116C, the direction of ΔF did not change monotonically with membrane potential. Furthermore, for superfusion in 100Na, the off-transition (return to the holding potential) evoked a rapid fluorescence quench followed by a transient tail relaxation that was superimposed on a relatively small steady-state ΔF during the voltage pulse. Qualitatively similar behavior was found when 1 mM P_i was also present in the superfusate although the rapid quench transient was less evident.

Normalized ΔF–V data for A104C and A116C are shown using the three superfusion conditions (100Ch, 100Na, and 100Na+1P_i) in Fig. 2 *B*. Unlike A116C and the four mutants characterized in our previous study (14), which all showed sigmoidal ΔF-V relationships that either monotonically increased or decreased with V, A104C showed a distinct minimum for each superfusion condition within the test potential range. According to our standard analysis procedure, the ΔF-V data for A116C were characterized by fitting with a Boltzmann relation (Eq. 3). After normalization to account for different expression levels, the data were adjusted such that the respective fits superimposed at the depolarizing limit (Fig. 2 *B*, *left panel*), where we assumed that all proteins were forced to occupy an inward-facing conformation, independent of the external substrate (Fig. 1 *A*). For A104C,

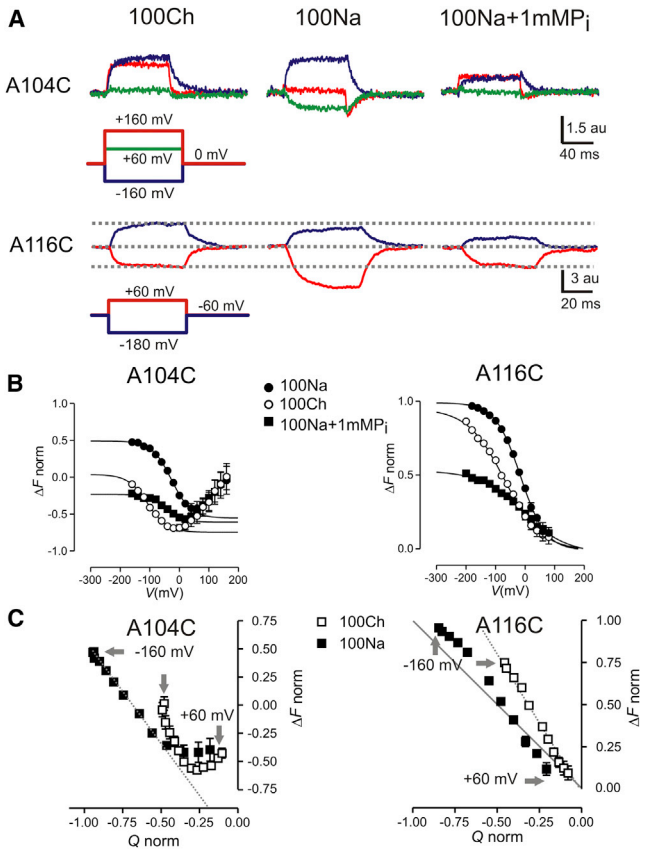

FIGURE 2 Voltage- and substrate-dependent changes in steady-state fluorescence intensity. (*A*) Recordings of changes in emitted fluorescence intensity for mutant A104C (*upper traces*) and A116C (*lower traces*) in response to voltage steps indicated for three superfusion conditions. Colors of ΔF traces correspond to same color for voltage pulses. Note that different holding potentials were used. (*B*) Voltage dependence of ΔF for A104C and A116C with three superfusion conditions (100Ch: *open circles;* 100Na *solid circles*; 100Na+1P_i *solid squares*). For A116C, data for individual oocytes were fit with Eq. 3 to obtain ΔF_{max} for 100Na and then normalized and offset so that they superimpose at the depolarizing extreme. The fit parameters were for 100Na (100Ch): ΔF_{max} = 1.00 ± 0.04 (0.96 ± 0.10); $V_{0.5}{}^{F}$ = −16 ± 3 mV (−69 ± 7 mV); and z^F = 0.59 ± 0.04 (0.40 ± 0.06). For A104C, data were fit from the hyperpolarizing limit to the minimum and normalized to ΔF_{max} before pooling ($n \geq 5$). The fit parameters were for 100Na (100Ch): ΔF_{max}=1.05 ± 0.04 (0.78 ± 0.08); $V_{0.5}{}^{F}$ −27 ± 3 mV (−107 ± 5 mV); and z^F = 0.76 ± 0.05 (0.75 ± 0.11). (*C*) Parametric plots of ΔF against charge displaced (Q from pooled, normalized data as in panel *B*), to indicate potential correlations between the corresponding data sets for superfusion in 100Na (*solid squares*) and 100Ch (*open squares*). For A104C (100Na, $V > 0$) and A116C (100Ch), linear relationships are evident (*dashed lines*). For A116C the 100-Na data deviate from the theoretical relationship with 100% correlation (*continuous line*). (*Arrows*) Membrane potential corresponding to the data point. To see this figure in color, go online.

we found that the data for each superfusion condition superimposed at the depolarizing limit. Both A104C and A116C showed a hyperpolarizing shift in the ΔF-V data in the absence of external Na^+ ions, and for A116C, the ΔF_{max} value reported by the fit remained unchanged in the absence of external Na^+. And for A104C, there was a 22% reduction in the predicted ΔF_{max}.

To test for correlations between the charge displacement (Q) and ΔF in the steady state, we plotted ΔF against Q parametrically for both mutants (Fig. 2 *C*). A linear relationship would suggest directly that both signals originate from the same underlying voltage-dependent process. Data sets were normalized to the respective Q_{max} and ΔF_{max} in 100Na. For superfusion in 100Ch, A116C showed an obvious linear relationship that passed through the origin, whereas the corresponding 100Na data deviated particularly at hyperpolarizing potentials such that for a given charge displacement, the measured ΔF exceeded the value expected if there were a strict 1:1 correlation. Mutant A104C also showed a linear relationship between ΔF and Q for 100Na at hyperpolarizing potentials that was offset from the origin; however, for 100Ch superfusion, there was no clear linear correlation.

We also determined the ΔF-V dependence at intermediate $[Na^+]_o$ (25, 50, and 75 mM (0 mM P_i)) (Fig. 3). By fitting these data with a Boltzmann function (Eq. 3) we obtained the midpoint voltage for fluorescence ($V_{0.5}{}^F$) and compared its dependence on $[Na^+]_o$ with the corresponding pre-steady-state relaxation data (Table 1). Like the pre-steady-state $V_{0.5}{}^Q$ dependence on $\log_{10}[Na^+]_o$, we also observed a linear relationship between $V_{0.5}{}^F$ and $\log_{10}[Na^+]_o$ for A104C and A116C with slopes comparable to the corresponding pre-steady-state data (Fig. 3 *B*, Table 1). These data points lay between data previously reported for labeling at Ser-155, Ser-226, Gln-319, and E451C (Fig. 1 *B*) (14).

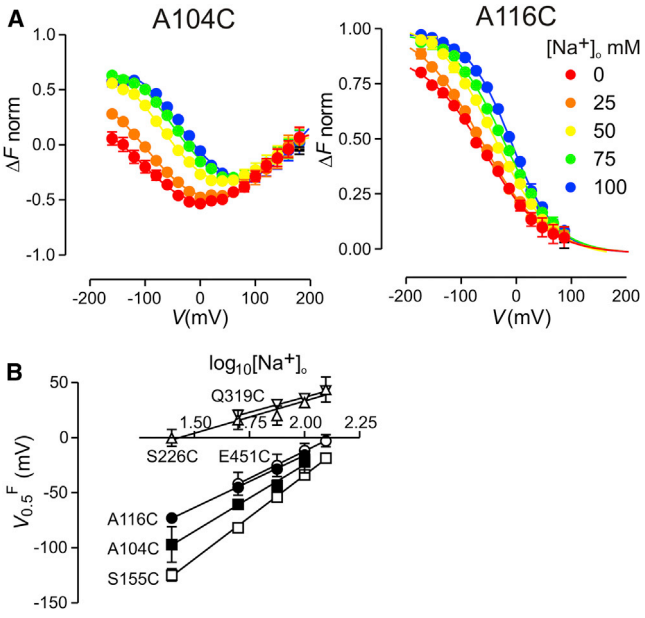

FIGURE 3 External Na^+ shifts the ΔF-V relationship for A104C and A116C. (*A*) Normalized ΔF-V data for A104C (*left*) and A116C (*right*) shown for selected $[Na^+]_o$ as indicated. (*Continuous lines*) Fits using Eq. 3. Note that for A104C, fits were between the hyperpolarizing limit and minimum ΔF. Normalized, pooled data were adjusted to superimpose at the depolarizing limit. (*B*) Relationships between midpoint voltages predicted from Boltzmann fit ($V_{0.5}{}^F$) and $\log_{10}[Na^+]_o$ for A104C and A116C in this study (*solid symbols*) and previously characterized mutants' (*open symbols*), with data redrawn from Virkki et al. (14). (*Straight lines*) Result of linear regression applied to data points (see Table 1 for slopes). To see this figure in color, go online.

Comparing the time course of pre-steady-state relaxations and fluorescence

In addition to the steady-state changes in ΔF that resulted from changing the membrane potential and superfusate (Figs. 2 and 3), we also observed that the time course of ΔF in response to voltage steps depended on the target membrane potential as well as the superfusing conditions. To compare the time course of ΔF and the pre-steady-state charge relaxations, we recorded current relaxations and fluorescence simultaneously from the same oocyte with the same recording bandwidth for each signal. During the pre-steady-state period, the time courses of the signals were described by single-exponential functions (see Materials and Methods) and the corresponding time constants, reported by the fit algorithm, were designated τ^Q (pre-steady-state charge displacement) and τ^F (fluorescence intensity), respectively. Fig. 4 *A* shows original traces and fits for a representative oocyte expressing A116C. For these experiments, we again focused on transitions between conformational states corresponding to previously indentified voltage-dependent partial reactions. We recorded data for superfusion in

1. 100Ch, assumed to allow only transitions associated with the empty carrier ($0 \leftrightarrow 1$) and internal Na^+ binding ($7 \leftrightarrow 0$); and
2. 100Na, assumed to include both the empty carrier and Na^+ interactions (transitions $7 \leftrightarrow 0 \leftrightarrow 1 \leftrightarrow 2 \leftrightarrow 3$) (Fig. 1 *A*).

Fig. 4 *B* shows plots of τ^Q and τ^F versus V under the two superfusing conditions (100Ch and 100Na) for A104C and A116C introduced in this study, together with previously unpublished data (I.C. Forster) for two mutants that gave sufficient temporal resolution for resolving ΔF at 500 Hz recording bandwidth (S155C and S226C (14)). In general, τ^Q and τ^F showed bell-shaped dependences on membrane potential and we observed the WT-like depolarizing shift in the peak of τ^Q in 100Na relative to 100Ch (e.g., Forster et al. (9)). For superfusion in 100Na, mutants A116C and S155C showed close agreement between both τ-values over the whole voltage range, whereas for A104C there was agreement only for depolarizing potentials. For superfusion in the absence of external Na^+ ions, agreement was found for A116C for $V > 0$ and for S155C over the entire voltage range. Mutant S226C showed τ^F values that were significantly slower than the corresponding τ^Q for both superfusion conditions. Poor signal resolution prevented reproducible estimations of τ^F for A104C in the intermediate potentials range.

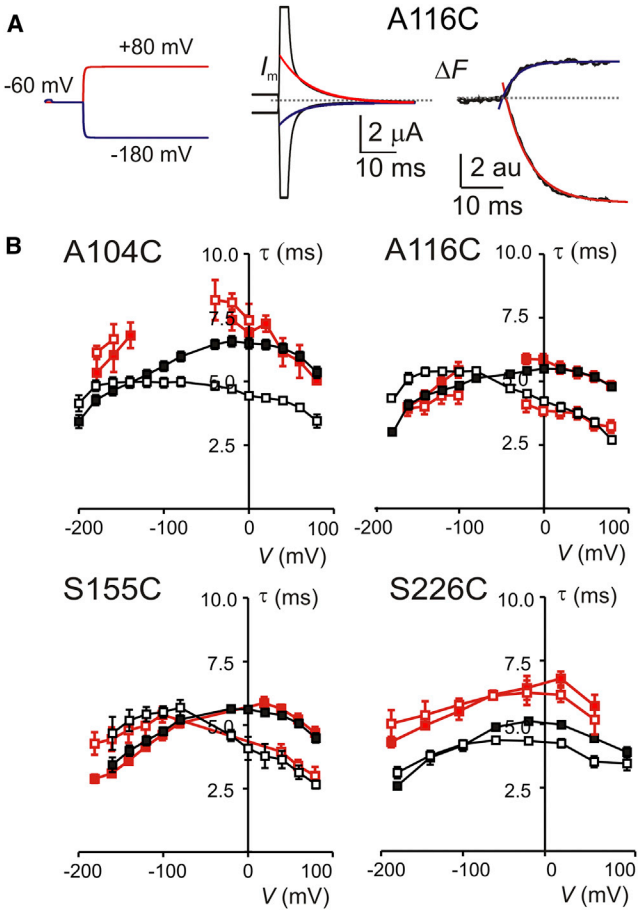

FIGURE 4 Comparison of time constants for current and ΔF. (*A*) Representative data from the same oocyte expressing A116C and labeled with MTS-TAMRA, in response to the voltage steps shown. Pre-steady-state current relaxation (*center panel*) and corresponding ΔF traces (*right panel*) show single exponential fits from which the time constants τ^Q and τ^F were obtained. Note that for this mutant, the same voltage step evokes opposite changes in the fluorescence and current. The recording bandwidth for both signals was 500 Hz. (*B*) Plots of τ^F (*red*) and τ^Q (*black*) against *V*, for four mutants indicated and superfusion in 100Ch (*open squares*) or 100Na (*solid squares*). Error bars are values reported from fits to pooled data ($n > 3$). Data points are joined for visualization. For A104C, we were unable to obtain reliable fits to the ΔF data in the range $-120 \leq V \leq -60$ mV. To see this figure in color, go online.

DISCUSSION

In this study, we compared pre-steady-state charge relaxations and changes in fluorometric intensity to investigate possible structure-function correlates between inferred local conformational changes and charge movement in response to rapid changes in membrane potential. We also combined data from previously identified sites (Ser-155, Ser-226, Gln-319, and Glu-451) (14) with data for the believed-new sites characterized here. For such a comparison to be useful, it is desirable for the mutagenesis and subsequent labeling to have minimal effect on the transport function so that behavior as close to WT behavior as possible, is retained. Indeed, with the exception of labeling Cys-144, the basic transport behavior was essentially unchanged at six externally accessible sites. The behavior of S144C was similar to that of a previously characterized S448C mutant (13) and reaffirms the functional importance of the two reentrant regions of NaPi-IIb in which these sites are located (Fig. 1 *B*). Moreover, accessibility to Cys-144 from the external medium was strongly dependent on the presence of Na^+, which suggested that this site became more exposed with Na^+ ions bound, thus implying a significant conformational change occurred with cation binding at −60 mV. Fig. 5 shows the predicted positions of five of the labeled sites investigated, superimposed on a three-dimensional model of human NaPi-IIa (23), and is consistent with their accessibility from the external medium.

Comparison between *Q* and ΔF in the steady state

Na^+-dependence

A104C and A116C, as well as the previously described mutants (S155C, S226C, Q319C, and E451C (14)), gave resolvable ΔF in response to voltage steps in the absence of external Na^+. This indicated that they sensed conformational changes associated with the empty carrier reorientation and internal Na^+ binding/debinding (Fig. 1 *A*). The

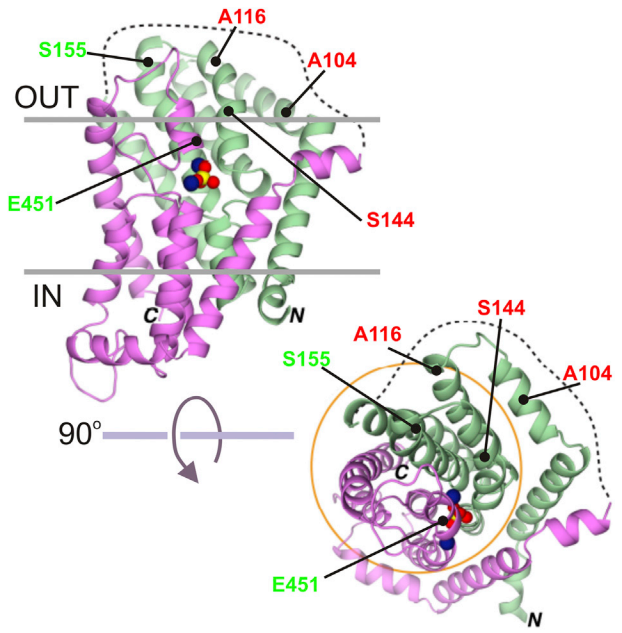

FIGURE 5 Location of sites of Cys substitution superimposed on a three-dimensional model of human NaPi-IIa (23). The protein is assumed to be in an outward-facing configuration with two of the three Na^+ ions (*blue*) and P_i (*yellow-red*) bound. (*Upper panel*) Side view; (*lower panel*) external-medium view. (*Dashed*) Large extracellular loop linking helices 3 and 4a (Fig. 1 *B*) with unknown fold. Sites S226 and Q319 within this loop were omitted. (*Circled*) Elements involved in the predicted transport domain. (*Green* and *pink regions*) Repeat units (Fig. 1 *B*). Modified from Fenollar-Ferrer et al. (23). To see this figure in color, go online.

addition of Na^+ ions to the external medium modified the voltage dependence of the pre-steady-state charge movements in a qualitatively similar fashion to that found for the WT (e.g., Forster et al. (9)), and we concluded that the electrogenic characteristics were not strongly influenced by either the mutagenesis or labeling. The fluorescence signals were also altered by external Na^+ ions, the extent of which depended on the labeling site.

To characterize the Na^+-dependence, we compared the variation of the respective midpoint voltages for charge ($V_{0.5}{}^{Q}$) and fluorescence ($V_{0.5}{}^{F}$) as $[Na^+]_o$ was varied. In the former case, this parameter represents an equilibrium potential for the voltage-dependent redistribution of mobile charges between extreme hyperpolarizing or depolarizing potentials. A feature of the pre-steady-state behavior of electrogenic SLC34 proteins is the linear relationship between $V_{0.5}{}^{Q}$ and $\log_{10}[Na^+]_o$ for large $[Na^+]_o$, and this appears to be a common kinetic feature for electrogenic cation-coupled transporters (24–28). For NaPi-IIb we have previously shown that a four-state kinetic model can account for this characteristic, whereby both the empty carrier and sequential binding of 2 Na^+ ions from the external medium before P_i contribute to the overall voltage dependence (19).

Simulations show that for 2 Na^+ ions binding sequentially, the limiting slope at high $[Na^+]_o$ approaches $\approx$120 mV/decade $[Na^+]_o$ at room temperature (19). We found reasonable agreement between the limiting slopes for charge and fluorescence for A104C, A116C, E451C, and S155C (Table 1). The similarity of the limiting slopes for charge and fluorescence indicated that the microenvironments of fluorophores at these sites experienced conformational changes directly related to the binding (and debinding) of multiple Na^+ ions. In contrast, two previously described mutants (S226C and Q319C (14)) showed significantly reduced slopes for the $V_{0.5}{}^{F}$ versus $\log_{10}[Na^+]_o$ plots. This reduced sensitivity of $V_{0.5}{}^{F}$ to changes in $[Na^+]_o$ suggested that the changes in fluorophore microenvironments at these sites do not directly reflect conformation changes associated with charge displacement, as for the other four mutants.

A five-state kinetic scheme accounts for the fluorescence emissions

To better understand the fluorescence behavior with respect to Na^+ interactions in the absence of external P_i, we performed kinetic simulations with a five-state model that included a recently identified single Na^+ ion interaction at the cytosolic interface (10) (Fig. 6 *A*). Rate constants describing the forward and backward transitions between the states were chosen based on previous kinetic simulations (e.g., Ghezzi et al. (11) and Andrini et al. (19)) to give reasonable agreement between the measured *Q-V* data and simulation (Fig. 6, *B* and *C*). Note that the simulations for each mutant are based on a model in which the electrogenic properties and rates for the partial reactions are fixed, and do not take account of any variations in voltage dependence between mutants that result from the mutagenesis and labeling (Table 1, see Fig. S2).

To simulate the voltage-induced changes in fluorescence, we assumed that the total F from a fixed population of transporters (N_t) can be expressed as: $F = N_t \sum af_n X_n$, where X_n is the probability of occupancy of state n and af_n values are coefficients representing the apparent fluorescence intensity associated with that state (7,29). This is the simplest phenomenological model that might reasonably account for the changes in fluorescence intensity but makes no prediction concerning the underlying mechanism. For example, changes in apparent fluorescence intensity might arise from shifts in the emission or absorption spectra, collisional quenching, etc. (e.g., Cha and Bezanilla (30)). With this caveat in mind, we determined a set of *af* values for each labeling site. If the fluorophore's microenvironment is different for each labeling site, the set of *af* values will also be unique for that mutant. By appropriate choice of *af* associated with each state, we could account for the general features of the voltage dependence ΔF, including the unique nonmonotonic characteristics of A104C, as well as previously published data for labeling at Ser-155, Ser-226, Gln-319, and E451C (14) (see Fig. S3).

We categorized the ΔF-*V* behavior according to whether apparent quenching occurred for depolarizing voltage steps (A116C and the previously described Q319C and E451C (14)) and hyperpolarizing voltage steps (S155C, S226C (14)) (see Fig. S3) or at intermediate potentials (A104C). For example, we emulated our measured ΔF-*V* data for A116C by assigning finite *af* values to States 1–3, whereas $af_0 = af_7 = 0$, which implies that when States 0 or 7 are occupied, the microenvironment of the fluorophore suppressed fluorescent emission. Moreover, to reduce the number of unknowns, we set $af_2 = af_3$. We found that the ratio $af_1/af_{2,3}$ was a critical determinant of the $V_{0.5}{}^{F}$ versus $\log_{10}[Na^+]_o$ slope (Fig. 6 *E*). Setting $af_1/af_{2,3} = 1.0$ gave a slope of 96 $\pm$ 4 mV/decade, close to that found experimentally for A116C (94 $\pm$ 1 mV/decade).

Because the fluorescence emission is expressed as the product of the probability of occupancy of a given state and its apparent fluorescence intensity, which varies according to the labeling site, the dependence of $V_{0.5}{}^{F}$ on $[Na^+]_o$ will not necessarily match that of $V_{0.5}{}^{Q}$. In the example simulations shown (Fig. 6 *D*) with the ratio $af_1/af_{2,3} < 1$, $V_{0.5}{}^{F}$ will be less sensitive to $[Na^+]_o$ because the partial reactions involving $[Na^+]_o$ contribute less to ΔF_{max} and the slope of $V_{0.5}{}^{F}$ versus $\log_{10}[Na^+]_o$ will be reduced compared with having $af_1/af_{2,3} \geq 1$ (Fig. 6, *D* and *E*). Moreover, for our model parameter set (see Fig. 6 legend), the simulations predict that the occupancy of State 2 was relatively unlikely (data not shown) when partial reaction $2 \leftrightarrow 3$ was very cooperative (19).

For mutants that showed apparent fluorescent quenching for hyperpolarizing voltage steps (S155C, S226C) (see

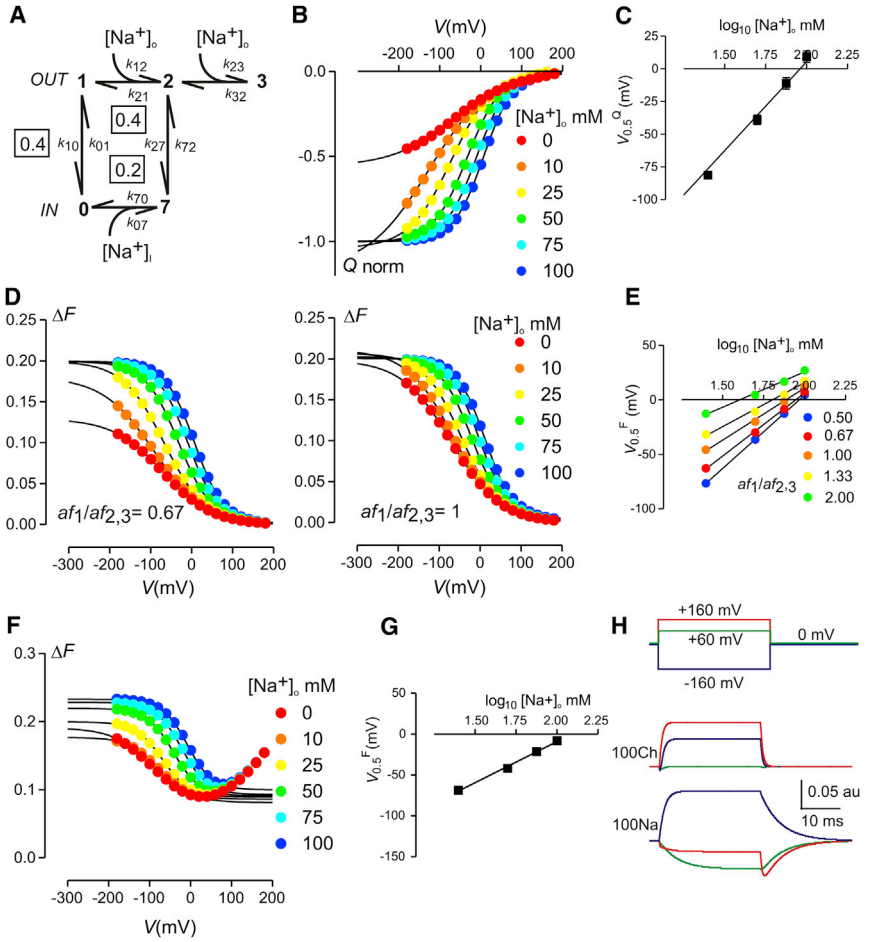

FIGURE 6 Simulations confirm fluorescence behavior. (*A*) Five-state kinetic scheme used to simulate pre-steady-state and fluorescence behavior. (*Boxed values*) Apparent valence of the corresponding partial reaction. The voltage dependence of these partial reactions was modeled by applying Eyring transition state theory to describe analytically the dependence of transition rate constants on membrane potential. Voltage-dependent partial reactions account for the movement of equivalent lumped charges that change conformational state by crossing a sharp, symmetrical energy barrier. The rate constants (in s^{-1}) were as follows: $k_{10} = 300\ \exp(-Vz_{10}\mu/2)$; $k_{01} = 100\ \exp(Vz_{10}\mu/2)$; $k_{12} = [Na^+]_o\ 2000\ \exp(-Vz_{12}\ \mu/2)$; $k_{21} = 500\ \exp(Vz_{12}\ \mu/2)$; $k_{23} = [Na^+]_o\ 8300$; $k_{32} = 100$; $k_{27} = 1$; $k_{07} = [Na^+]_i\ 2000\ \exp(Vz_{07}\ \mu)$; $k_{70} = 500\ \exp(-Vz_{07}\ \mu)$; $k_{27} = 1$; and $\mu = e/kT \approx 40\ V^{-1}$ at 20°C; $z_{10} = 0.4$; $z_{12} = 0.4$; and $z_{07} = 0.2$. Rate constant k_{72} was defined independently in terms of the other rate constants under conditions of zero driving force to satisfy detailed balance for the leak cycle. We assumed $[Na^+]_i = 0.02$ M. (*B*) Simulated *Q-V* data using the model parameter set given in panel *A* for the $[Na^+]_o$ value indicated. (*Continuous lines*) Fits with Eq. 3. (*C*) Relationships between $V_{0.5}^{Q}$ and $\log_{10}[Na^+]_o$ values for the simulated data in *B*. A linear regression fit to these data yielded a slope of 115 ± 4 mV/decade. (*D*) Simulated Δ*F-V* data using the model in panel *A* with two sets of apparent fluorescence intensities: $af_0 = 0$, $af_1 = 0.2$, $af_2 = af_3 = 0.3$, $af_7 = 0$ (*left panel*); $af_0 = 0$, $af_1 = af_2 = af_3 = 0.2$, $af_7 = 0$, (*right panel*) and indicated $[Na^+]_o$. (*Continuous lines*) Fits with Eq. 3. The simulations with $af_1/af_{2,3} = 1$ best described the behavior of A116C. (*E*) The midpoint voltage for simulated Δ*F* ($V_{0.5}^{F}$) shows a linear dependence on $[Na^+]_o$ with slopes that depend on the relative apparent fluorescence intensity between State 1 and States 2 and 3, as indicated. Slopes vary from 135 ± 1 mV/decade ($af_1/af_{2,3} = 0.5$) to 65 ± 4 mV ($af_1/af_{2,3} = 2.0$). The data set with $af_1/af_{2,3} = 1.0$ matched the behavior of mutant S116C with a slope of 96 ± 4 mV/decade (see panel *D*, *right panel* and Fig. 3 *A*, *right panel*). (*F*) Simulations recapitulate the behavior of A104C (compare with Fig. 3 *A*). (*Continuous lines*) Fits with Eq. 3 from hyperpolarizing limit to minimum for each data set. The set of apparent fluorescence intensities for the five states was as follows: $af_0 = 0.02$, $af_1 = 0.2$, $af_2 = 0.1$, $af_3 = 0.25$, and $af_7 = 0.55$. (*G*) The midpoint voltage of the A104C simulation ($V_{0.5}^{F}$) shows a linear dependence on $[Na^+]_o$ with slope: 101 ± 5 mV/decade. (*H*) Simulations of A104C fluorescence behavior recapitulate the transient behavior as seen in representative data (Fig. 2 *A*). The same colors are used for the voltage step and simulated fluorescence. To see this figure in color, go online.

Virkki et al. (14)), we obtained close agreement between measurement and simulations if nonzero *af* values were assigned to the inward-facing states (0, 1, and 7) (Table 2, and see Fig. S3). For example, our simulations revealed that mutant S226C, which shows a relatively weak dependence of V_{05}^{F} on $[Na^+]_o$ (Table 1), would give the highest fluorescence signal when occupying State 7 (internal Na^+ bound) with a depolarized membrane. For a hyperpolarizing voltage step, and increasing $[Na^+]_o$, the state occupancies will redistribute and movement out of States 7 and 0 will be accompanied by a decrease in emitted fluorescence. For mutant S155C, it was necessary to assign some fluorescence to State 1 to account for the following:

1. The reduced fluorescence quenching in the absence of external Na^+; and
2. The increased $V_{0.5}^{F}$ versus $\log_{10}[Na^+]_o$ slope, as observed experimentally.

Finally, to reproduce the biphasic characteristic of the Δ*F-V* data for A104C (Fig. 3 *A*), we assigned nonzero *af* values to all five states of the kinetic scheme (Table 2). The simulations with these parameters predicted the voltage dependence of Δ*F* in the steady-state (Fig. 6 *F*) and the shift in $V_{0.5}^{F}$ for hyperpolarizing potentials as $[Na^+]_o$ decreased (compare Fig. 6 *G* with Fig. 3 *B*). Thus, the fluorescence emitted by the fluorophore at Cys-104 reflects both inward and outward state occupancies as the imposed membrane potential is varied from strong depolarization to strong hyperpolarization, respectively. The simulations could also successfully recapitulate the unique time-dependent relaxations observed when making a return voltage step from the depolarizing limit (Fig. 6 *H* and compare with Fig. 2 *A*). At +160 mV, a fraction of transporters occupy State 7 and a hyperpolarizing membrane potential step results in transporters leaving this state and redistributing between the

TABLE 2 Comparison of fractional apparent fluorescence intensities

	State				
Mutant	7	0	1	2	3
A104C	0.49	0.02	0.18	0.09	0.22
A116C	0	0	0.33	0.33	0.33
S155C	0.38	0.38	0.24	0	0
S226C	0.80	0.20	0	0	0
Q319C	0	0.16	0.32	0.26	0.26
E451C	0	0.05	0.24	0.24	0.47

For each mutant and a given state, the fractional apparent fluorescence intensity (*af*) was calculated from the ratio of apparent fluorescence intensity for that state, divided by the sum of the apparent *af* values for each state. The value of *af* was determined by trial and error to yield a best visual match between the experimental data and simulations using the kinetic scheme (Fig. 6 *A*). The same kinetic parameter set was assumed for each mutant (see legend, Fig. 6).

other states. The initial rapid quenching represents movement to State 0, which has a small *af*, and the slower relaxing increase in fluorescence represents the reorientation of the empty carrier to State 1 and eventual occupancy of State 3 (with 2 Na^+ ions bound).

The steady-state fluorescence behavior for all six mutants was summarized by generating a set of *af* values for each that gave a good match to the experimental data (Table 2). For a given mutant, the table entries indicate a relative measure of the change in the microenvironment of the respective fluorophore when the protein occupies each of the 5 states. Thus, for labeling, at Cys-104 the largest fluorescence emission occurs when the transporters are inward-facing with Na^+ bound or outward-facing with and without Na^+ bound. Thus, the fluorophore at Cys-104 experiences apparent quenching at intermediate states (0, 1) and reports behavior consistent with an alternating access model. This would also accord with its predicted location adjacent to the core transport domain (Fig. 5). Fluorophores at Cys-116, Cys-319, and Cys-451 report occupancy of outward-facing states and also the inward-facing empty carrier (for Cys-319 and Cys-451).

These sites are predicted to be within the transport domain (Fig. 5) and the differences in their ΔF-V characteristics suggested that their microenvironments respond according to the relative movements of helical domains and linkers to which they are associated, as cations bind and debind. For the labeled Cys-116, we modeled the same *af* for States 1–3, and could thereby account for the experimentally observed invariance of ΔF_{max} when superfusing with 100Ch and 100Na (Fig. 2 *B*). It was significant that the voltage dependence of fluorescence emission from labeled Cys-155 and Cys-226 complemented that for labeled Cys-116 and Cys-319. If ΔF values were a result of changes in the polarity of the fluorophore's microenvironment, the complementary ΔF-V for A116C and S155C suggested that the respective sites move in a reciprocal manner relative to one another into more or less polar environments respectively, as we have previously proposed for the pairs Cys-155/Cys-451 and Cys-226/Cys-319 (14).

Phosphate dependence

All mutants gave resolvable voltage-dependent ΔF when saturating P_i (1 mM) was superfused with 100 mM external Na^+. For the new mutants A104C and A116C, fluorescence was quenched for hyperpolarizing potentials relative to the emission level in100Na. This established that in the cotransport mode, the fluorophores at these sites reported a different change in their microenvironment from when only Na^+ was present. For strong membrane depolarization, the fluorophore at Cys-104 reported the same ΔF, independent of the superfusing condition (Fig. 2 *B*). Based on the above simulations, this suggested that only inward conformations associated with States 0 and 7 were reported under these conditions. Despite quenching of ΔF in the presence of P_i, the voltage dependence of ΔF was qualitatively similar for both A104C and A116C and showed the same sigmoidal dependence for $V < 0$.

Thus, the quenching behavior of fluorophores at Cys-104 and Cys-116 for hyperpolarizing potentials suggests that the relative changes in the fluorophore's microenvironment remain unchanged and largely reflect voltage-dependent conformational changes associated with the external cation interactions. However, for a given membrane potential in the hyperpolarizing range, occupancy of States 4–6 (Fig. 1 *A*), for which we would predict small apparent fluorescence intensities, is now favored and therefore the relative fluorescence emission is accordingly reduced. The P_i-dependence ΔF-V could, in principle, be quantified by extending the five-state scheme to include the complete cotransport cycle; however, with such a large number of free parameters and unknown internal rate constants, it would be difficult to determine a unique set of apparent fluorescence intensities with confidence.

Comparison of the time-resolved charge movement and ΔF

We reasoned that if the conformational changes purportedly shown by the fluorophore were directly related to those associated with the charge movement, a correlation between τ^Q and τ^F should exist. Only one mutant (S155C) fulfilled this criterion for both superfusion conditions and over a wide potential range. This suggested that the conformational changes reported by the fluorophore at Cys-155 directly reflect those accompanying the charge movements associated with the empty carrier and cation interactions for both inward and outward conformations. Like S155C, when external Na^+ ions were present in the superfusate, A104C and A116C also showed reasonable agreement between τ^Q and τ^F for $V > 0$. According to our model, most of the charge movement associated with a depolarizing

voltage step arises from Na^+ ions leaving their binding sites and the reorientation of the empty carrier.

The agreement between τ^Q and τ^F indicates that the fluorophores at these sites report the same dynamics for the accompanying conformational change as the proteins leave State 3. In general, however, deviations between τ^Q and τ^F would be expected because fitting the relaxations with a single exponential is strictly only applicable to a two-state system. The discrepancy between τ^F and τ^Q for mutant S226C might be similarly explained by our inability to resolve a slower component in the pre-steady-state relaxation associated with the transitions to and from State 7, the occupancy of which, according to our model, results in the highest apparent fluorescence intensity.

CONCLUSIONS

We present evidence that sites in an electrogenic Na^+-coupled P_i cotransporter are involved in specific molecular rearrangements that reflect the influence of membrane potential and availability of external Na^+ ions. Labeling had only marginal effect on transport function for the six sites explored here, and we therefore assume that the conformational changes reported by the changes in fluorescence emission closely represent WT behavior. In the absence of external P_i, a five-state kinetic scheme can account for the behavior in terms of charge movement and changes in fluorescence intensity. By assigning an apparent fluorescence intensity to each state, we could interpret the steady-state fluorescence signal in terms of the state-dependent molecular rearrangements unique to the labeling site.

Our findings also provide indirect evidence in support of an alternating access mechanism, whereby the probability of the cation binding sites being exposed to the external or internal media is governed by the imposed membrane potential. Furthermore, by comparing the time course of fluorescence changes and charge movement, we could identify those parts of the protein that undergo conformational changes in response to changes in membrane potential. This approach of combining charge relaxation kinetics and time-resolved fluorescence should find application for other electrogenic cotransporters to elucidate their structure-function relationships under physiological conditions, particularly if three-dimensional structural data is available.

SUPPORTING MATERIAL

Three figures are available at http://www.biophysj.org/biophysj/supplemental/S0006-3495(14)00267-7.

We thank Eva Hänsenberger for oocyte preparation and Drs. Don Loo and Edune Gorraitz (University of California at Los Angeles) and Anne-Kristine Meinild (University of Zurich) for critical comments on the manuscript.

Financial support was provided by the Swiss National Science Foundation (to I.C.F.).

REFERENCES

1. Forrest, L. R., R. Krämer, and C. Ziegler. 2011. The structural basis of secondary active transport mechanisms. *Biochim. Biophys. Acta.* 1807:167–188.
2. Zhao, Y., D. S. Terry, …, J. A. Javitch. 2011. Substrate-modulated gating dynamics in a Na^+-coupled neurotransmitter transporter homologue. *Nature.* 474:109–113.
3. Koch, H. P., and H. P. Larsson. 2005. Small-scale molecular motions accomplish glutamate uptake in human glutamate transporters. *J. Neurosci.* 25:1730–1736.
4. Akyuz, N., R. B. Altman, …, O. Boudker. 2013. Transport dynamics in a glutamate transporter homologue. *Nature.* 502:114–118.
5. Claxton, D. P., M. Quick, …, H. S. McHaourab. 2010. Ion/substrate-dependent conformational dynamics of a bacterial homolog of neurotransmitter:sodium symporters. *Nat. Struct. Mol. Biol.* 17:822–829.
6. Loo, D. D., B. A. Hirayama, …, E. M. Wright. 1998. Conformational changes couple Na^+ and glucose transport. *Proc. Natl. Acad. Sci. USA.* 95:7789–7794.
7. Loo, D. D., B. A. Hirayama, …, E. M. Wright. 2006. Conformational dynamics of hSGLT1 during Na^+/glucose cotransport. *J. Gen. Physiol.* 128:701–720.
8. Meinild, A. K., B. A. Hirayama, …, D. D. Loo. 2002. Fluorescence studies of ligand-induced conformational changes of the Na^+/glucose cotransporter. *Biochemistry.* 41:1250–1258.
9. Forster, I. C., N. Hernando, …, H. Murer. 2012. Phosphate transport kinetics and structure-function relationships of SLC34 and SLC20 proteins. *Curr. Topics Membr.* 70:313–356.
10. Patti, M., C. Ghezzi, and I. C. Forster. 2013. Conferring electrogenicity to the electroneutral phosphate cotransporter NaPi-IIc (SLC34A3) reveals an internal cation release step. *Pflugers Arch.* 465:1261–1279.
11. Ghezzi, C., A. K. Meinild, …, I. C. Forster. 2011. Voltage- and substrate-dependent interactions between sites in putative re-entrant domains of a Na^+-coupled phosphate cotransporter. *Pflugers Archiv. Eur. J. Phycol.* 461:645–663.
12. Ghezzi, C., H. Murer, and I. C. Forster. 2009. Substrate interactions of the electroneutral Na^+-coupled inorganic phosphate cotransporter (NaP_i-IIc). *J. Physiol.* 587:4293–4307.
13. Virkki, L. V., H. Murer, and I. C. Forster. 2006. Voltage clamp fluorometric measurements on a type II Na^+-coupled P_i cotransporter: shedding light on substrate binding order. *J. Gen. Physiol.* 127:539–555.
14. Virkki, L. V., H. Murer, and I. C. Forster. 2006. Mapping conformational changes of a type IIb Na^+/P_i cotransporter by voltage clamp fluorometry. *J. Biol. Chem.* 281:28837–28849.
15. Cha, A., N. Zerangue, …, F. Bezanilla. 1998. Fluorescence techniques for studying cloned channels and transporters expressed in *Xenopus* oocytes. *Methods Enzymol.* 296:566–578.
16. Forster, I. C., C. A. Wagner, …, A. Werner. 1997. Electrophysiological characterization of the flounder type II Na^+/P_i cotransporter (NaP_i-5) expressed in *Xenopus laevis* oocytes. *J. Membr. Biol.* 160:9–25.
17. Loo, D. D., B. A. Hirayama, …, E. M. Wright. 2005. Perturbation analysis of the voltage-sensitive conformational changes of the Na+/glucose cotransporter. *J. Gen. Physiol.* 125:13–36.
18. Meinild, A. K., D. D. Loo, …, N. MacAulay. 2009. Elucidating conformational changes in the γ-aminobutyric acid transporter-1. *J. Biol. Chem.* 284:16226–16235.
19. Andrini, O., A. K. Meinild, …, I. C. Forster. 2012. Lithium interactions with Na+-coupled inorganic phosphate cotransporters: insights into the mechanism of sequential cation binding. *Am. J. Physiol. Cell Physiol.* 302:C539–C554.
20. Ehnes, C., I. C. Forster, …, H. Murer. 2004. Structure-function relations of the first and fourth extracellular linkers of the type IIa Na^+/P_i cotransporter: II. Substrate interaction and voltage dependency of two functionally important sites. *J. Gen. Physiol.* 124:489–503.
21. Karlin, A., and M. H. Akabas. 1998. Substituted-cysteine accessibility method. *Methods Enzymol.* 293:123–145.

22. Ehnes, C., I. C. Forster, …, H. Murer. 2004. Structure-function relations of the first and fourth predicted extracellular linkers of the type IIa Na^+/Pi cotransporter: I. Cysteine scanning mutagenesis. *J. Gen. Physiol.* 124:475–488.

23. Fenollar-Ferrer, C., M. Patti, …, L. R. Forrest. 2014. Structural fold and substrate binding sites of the human Na^+-phosphate cotransporter NaP_i-II. *Biophys. J.* 106:1268–1279.

24. Meinild, A. K., and I. C. Forster. 2012. Using lithium to probe sequential cation interactions with GAT1. *Am. J. Physiol. Cell Physiol.* 302:C1661–C1675.

25. Hazama, A., D. D. Loo, and E. M. Wright. 1997. Pre-steady-state currents of the rabbit Na^+/glucose cotransporter (SGLT1). *J. Membr. Biol.* 155:175–186.

26. Mager, S., Y. Cao, and H. A. Lester. 1998. Measurement of transient currents from neurotransmitter transporters expressed in *Xenopus* oocytes. *Methods Enzymol.* 296:551–566.

27. MacKenzie, B., D. D. Loo, …, E. M. Wright. 1996. Mechanisms of the human intestinal H^+-coupled oligopeptide transporter hPEPT1. *J. Biol. Chem.* 271:5430–5437.

28. Loo, D. D., X. Jiang, …, E. M. Wright. 2013. Functional identification and characterization of sodium binding sites in Na symporters. *Proc. Natl. Acad. Sci. USA.* 110:E4557–E4566.

29. Larsson, H. P., A. V. Tzingounis, …, M. P. Kavanaugh. 2004. Fluorometric measurements of conformational changes in glutamate transporters. *Proc. Natl. Acad. Sci. USA.* 101:3951–3956.

30. Cha, A., and F. Bezanilla. 1998. Structural implications of fluorescence quenching in the *Shaker* K^+ channel. *J. Gen. Physiol.* 112: 391–408.

31. Mancusso, R., G. G. Gregorio, …, D. N. Wang. 2012. Structure and mechanism of a bacterial sodium-dependent dicarboxylate transporter. *Nature.* 491:622–626.